Stellar Population Ordering from Galactic Dynamics

Nicolas Poupart[1]

[1]Independent Researcher, Quebec, Canada
[*]Corresponding author. E-mail: nicolas.poupart@yahoo.fr

Abstract. We investigate whether stellar population information can be recovered from galactic dynamics. Starting from observed rotation curves, we construct synthetic stellar population mixtures constrained to reproduce the effective mass distribution. From these populations, we compute ultraviolet and optical colors and compare them to GALEX and SDSS observations.

We find statistically significant correlations between predicted and observed color indices across multiple bands, including FUV–NUV, $g - r$, $r - z$, and NUV–r. Rank–rank correlations reach significances up to $\gtrsim 5\sigma$, indicating that the ordering of stellar populations is encoded in the dynamical information. These results show that rotation curves contain non–trivial information about stellar population structure beyond their standard interpretation as mass tracers.

This behavior is consistent with a picture in which the effective dark mass component reflects gravitational binding energy, linking dynamics and stellar population properties.

Keywords. Galaxy kinematics and dynamics—Stellar populations—Galaxy photometry—Ultraviolet observations—Statistical methods—Rotation curves—Dark matter

1. Introduction

The origin of the dark mass component inferred from galactic dynamics remains one of the central open questions in astrophysics (Courteau *et al*., 2014). While the presence of an additional mass component is robustly established through rotation curves and dynamical modeling (Rubin *et al*., 1980; Persic *et al*., 1996), its physical nature is still unknown.

At the same time, galaxies exhibit well-defined correlations between their dynamical properties and their photometric observables (Bell & de Jong, 2001; McGaugh *et al*., 2000, 2016), which are commonly used to infer stellar masses and population properties from photometric data (Taylor *et al*., 2011). However, these relations are typically interpreted as empirical correlations, without a direct physical mechanism linking the dynamical mass distribution to the ordering of stellar populations.

This separation between dynamics and photometry motivates investigating whether the dynamical mass distribution itself can encode information about the structure of stellar populations.

In this work, we address this question by constructing an explicit mapping between dynamical mass distributions and photometric observables. Rather than relying on empirical fitting relations, we introduce a physically motivated estimator based on the gravitational binding energy of the system. This quantity is computed directly from the mass distribution and provides a scalar measure that can be used to reconstruct stellar population properties.

We show that this approach leads to strong and statistically robust correlations between predicted and observed photometric quantities. In particular, optical and UV–optical colors exhibit a clear monotonic ordering, while the ultraviolet regime displays more complex behavior. These results are validated through extensive bootstrap resampling and non-parametric permutation tests.

Importantly, the reconstructed relations are not driven by the tested observational systematics such as inclination or morphology, and remain stable across multiple subsamples. This suggests that the observed ordering reflects a property of the underlying mass distribution.

These results indicate that the effective dark mass component inferred from galactic dynamics may be interpreted, at least in part, as gravitational binding energy. While this work does not constitute a complete theoretical description of dark matter, it provides quantitative support for a physical interpretation in which gravitational energy may contribute to the effective mass budget of galaxies.

2. Data and Sample Selection

This work is based on the SPARC galaxy sample (Lelli *et al.*, 2016), which provides high-quality rotation curves derived from resolved kinematic data together with near-infrared photometry and structural parameters. All galaxies included in the SPARC database are retained in the dynamical analysis. No selection or rejection is applied on the basis of SPARC photometric quality, since the SPARC photometry is used exclusively for the construction of rotation curves and baryonic mass distributions.

Observed galaxy colors are obtained from external ultraviolet and optical surveys. Ultraviolet photometry is taken from the GALEX mission (Martin *et al.*, 2005; Bianchi *et al.*, 2011), while optical colors are drawn from the SDSS survey (York *et al.*, 2000; Fukugita *et al.*, 1996). As a consequence, the effective sample size is determined by the availability of GALEX and SDSS measurements for a given galaxy, and not by any filtering of the SPARC dataset itself. Depending on the color index considered, the number of galaxies available for the correlation analysis ranges from approximately $N \simeq 120$ to $N \simeq 140$. The exact number of objects used is explicitly reported for each color.

Four integrated color indices are analyzed in this work: $r - z$, $g - r$, FUV − NUV, and NUV − r. Observed colors are taken directly from the GALEX and SDSS catalogues using their standard photometric calibrations. No additional extinction or inclination-dependent corrections are applied beyond those already incorporated in the original survey calibrations.

For each galaxy, a broad set of global physical parameters is available or computable from the SPARC database, including the total baryonic mass $M_{\rm bar}$, quantities from which the dark mass component $M_{\rm dark}$ is derived, disk and bulge luminosities, mass-to-light ratios, surface brightnesses, characteristic radii, inclination angle, Hubble morphological type, and other derived photometric and kinematic quantities. In the present work, only inclination and morphological type are used as control variables for statistical robustness tests. All other global parameters are not employed in the analysis.

Predicted stellar population properties (Conroy, 2013) are computed independently from the observed colors, using exclusively the dynamical information encoded in the galactic rotation curves. To minimize methodological ambiguity, we restrict the reconstruction to the outermost resolved kinematic point of each galaxy, which provides a single global constraint on the total baryonic and inferred dark mass. This allows the reconstruction problem to be formulated in a simplified form, without radial propagation or sequential path dependence. The reconstruction therefore relies only on the pair $(M_{\rm bar}, M_{\rm dark})$ derived from this outermost point.

No photometric, spectroscopic, or stellar population information is used at any stage of the reconstruction procedure.

From these reconstructed stellar populations, predicted integrated colors are derived. Color residuals are defined throughout this work as:

$$\Delta C = C_{\rm obs} - C_{\rm pred} \tag{1}$$

Galaxies are grouped into three broad morphological classes based on their Hubble type, corresponding to early-type disks (S0–Sb), late-type disks (Sbc–Sdm), and irregular systems (Sm–BCD). This classification is used solely for robustness and consistency checks and does not enter the construction of the predicted stellar populations.

Galaxy inclinations i are taken directly from the SPARC catalogue, where they are derived using standard photometric and kinematic methods (Tully *et al.*, 1998). To assess possible projection or extinction-related systematics, the sample is additionally divided into three inclination ranges: low-inclination systems ($i < 45°$), intermediate-inclination systems ($45° \leq i < 70°$), and high-inclination systems ($i \geq 70°$). Inclination is treated strictly as a control variable and plays no role in the prediction of galaxy colors.

2.1 *Predicted Photometric Quantities*

Once the stellar population has been reconstructed from the dynamical constraints alone, its integrated photometric properties are computed. This step constitutes a forward modeling stage, in which the reconstructed population is translated into observable quantities without any additional adjustment beyond the adopted stellar population synthesis prescriptions.

For each stellar component of the reconstructed population, standard stellar population synthesis models (Bruzual & Charlot, 2003; Conroy *et al.*, 2009) are used to assign spectral energy distributions consistent with the corresponding stellar type. The total emission of a galaxy is then obtained by summing the contributions of all components, weighted by their reconstructed mass fractions.

From the resulting integrated spectrum, global photometric quantities are derived, including ultraviolet and optical colors. In particular, the color indices FUV–NUV, $g - r$, $r - z$, and NUV–r are computed in a self-consistent manner. These predicted colors depend only on the reconstructed stellar population and do not involve any photometric input from the observed data.

More specifically, the reconstruction relies only

on the radial distribution of the baryonic mass and the missing mass component required to reproduce the observed dynamics, i.e. the set of points $(M_{\rm bar}(r), M_{\rm dark}(r), r)$ inferred from the rotation curve. The predicted photometric quantities therefore constitute direct outputs of the model, which are subsequently compared to the observed GALEX and SDSS measurements in an a posteriori manner.

The predicted photometric quantities are compared to the observed GALEX and SDSS measurements using a set of complementary statistical indicators designed to assess both the strength and the robustness of the inferred relations. All statistical analyses are performed on global galaxy-integrated quantities.

The primary level of comparison relies on correlation analyses between predicted and observed colors. Both Pearson linear correlation coefficients (Pearson, 1895) and Spearman rank-order correlation coefficients (Spearman, 1904) are computed. The Pearson coefficient probes linear associations in the raw photometric space, while the Spearman coefficient is sensitive to monotonic ordering independently of the absolute scaling. The significance is expressed as a Gaussian-equivalent sigma derived from the two-sided p-value of the Student's t-statistic (with N-2 degrees of freedom).

3. Exact Gravitational Binding Energy

We now introduce the computation scheme used throughout this work to evaluate the effective gravitational binding energy. The objective is not to revisit the full theoretical construction developed previously (Poupart, 2025, 2026), but rather to formalize a calculation procedure that is both explicitly reproducible and independent of any algorithmic ordering of stellar populations. This estimator constitutes the central physical quantity used in the reconstruction procedure.

In standard formulations, gravitational potential energy is defined relative to an arbitrary reference level, typically taken at infinity. Consequently, the associated binding energy depends on this convention and on how the system is defined.

This leads to a conceptual ambiguity: the term "potential", which originally refers to the potential to perform work, does not correspond here to the actual work that can be extracted from the energy stored in the system, but rather to the energy required to perform a given operation on this system, such as moving its constituents to infinity.

The fact that the total gravitational energy of a system is not well defined is closely related to the fact that mass itself is not an absolute quantity within the framework of relativity. The problem was first clearly formulated in terms of classical mass renormalization by (Brillouin, 1964, 1965), and later addressed in the context of general relativity by (Hawking, 1968). The Hawking mass provides a geometrical definition of mass that includes gravitational energy, which is conceptually close to a mass renormalized by potential energy, although the underlying formalism is different. Related definitions of gravitational energy and effective mass in general relativity have also been explored in spherically symmetric systems (Misner & Sharp, 1964; Hayward, 1996). This remains an important open question.

Works exploring the hypothesis that such a renormalization of mass or spacetime by gravitational energy could account for the missing dark mass are relatively scarce. In addition to exploratory studies by the author (Poupart, 2014, 2017a,b), we note the work of Deur (Deur, 2019; Deur *et al*., 2020; Deur, 2021, 2022), who argues (numerically) that the self-interaction of the gravitational field through its own energy density can generate a spacetime curvature capable of mimicking an additional dark mass component. However, these approaches do not provide a simple analytical description of cosmological phenomena. They nevertheless illustrate how gravitational binding energy can produce additional curvature that may be interpreted either as an effective mass or as a renormalization of mass.

Here, we instead consider the physically meaningful energy associated with the formation of the system, namely the total energy released during the collapse or assembly of its constituent matter.

This defines the effective gravitational binding energy used throughout this work. This definition removes the ambiguity associated with arbitrary reference levels and provides a physically grounded estimator of gravitational energy.

3.1 *Additive Construction of the Binding Energy*

Consider a system M decomposed into n mass intervals characterized by densities ρ_i and total masses M_i. Each interval is constructed from individual self-gravitating stars sharing the same density and is then treated as an equivalent compact sphere whose radius follows directly from mass conservation:

$$R_i = \left(\frac{3M_i}{4\pi\rho_i}\right)^{1/3} \tag{2}$$

The gravitational binding energy associated with this compact configuration defines a natural energy scale:

$$\Delta E_i = \frac{3G}{5}\frac{M_i^2}{R_i} \tag{3}$$

This contribution depends only on intrinsic properties of the interval and therefore enters the total energy as a formally additive term. The global configuration obtained after combining all intervals is defined by mass and volume conservation:

$$M = \sum_{i=1}^{n} M_i, \qquad R^3 = \sum_{i=1}^{n} R_i^3 \tag{4}$$

The contributions over all intervals yield the total energy:

$$\Delta E_{\text{tot}} = \sum_{i=1}^{n} \Delta E_i + \frac{3G}{5}\frac{M^2}{R} \tag{5}$$

The final term represents the binding energy of the global compact configuration obtained after all mergers. In practice, it remains of the same order of magnitude as the individual interval contributions and therefore does not dominate the total energy, typically accounting for only a few percent (typically $1\% - 10\%$).

This construction defines a complete and self-consistent estimate of the effective gravitational binding energy associated with the system. Having established its explicit form, we now examine its physical and mathematical properties, as well as its implications for the reconstruction procedure.

3.2 *Consistency of the Energy Estimate*

The proposed evaluation of the effective gravitational binding energy is supported by three complementary arguments.

First, it follows directly from a physically grounded construction applied consistently across scales. The energy scale GM^2/R is obtained by starting from individual stars, each treated as a self-gravitating sphere, and by aggregating them into compact configurations through volume-conserving mergers. Stellar populations are therefore not introduced as abstract blocks but emerge from the same physical logic that governs the elementary constituents. The conservative nature of the gravitational field ensures that the resulting binding energy depends only on the final configuration and not on the assembly path, while volume conservation prevents the introduction of artificial forces or unphysical density variations. The calculation thus remains firmly anchored in standard gravitational physics.

Second, the method possesses a consistent mathematical structure. The total energy is obtained through formally additive contributions, while the final result is invariant under permutation of the mass intervals. This dual property guarantees that the estimate is independent of any arbitrary ordering of stellar populations and therefore reflects an intrinsic property of the mass distribution rather than an artifact of the algorithm.

Third, the approach demonstrates empirical adequacy. When applied to observed stellar populations, the resulting energy scale is consistent with SPARC-based reconstructions and GALEX/SDSS photometric validations. This convergence between theoretical construction and observational constraints provides an additional indication that the estimator captures the main features of the gravitational physics at galactic scales.

3.3 *Algorithmic Structure*

Although the construction can be written as a sequential aggregation, the resulting energy depends only on the collection $\{(M_i, \rho_i)\}$ and not on the order in which the intervals are processed. Formally, let σ be any permutation of $\{1, \ldots, n\}$. The cumulative radius after all mergers satisfies:

$$R^3 = \sum_{i=1}^{n} R_{\sigma(i)}^3 = \sum_{i=1}^{n} R_i^3 \tag{6}$$

which implies that the final compact state (M, R) is uniquely defined. Since the additive contributions ΔE_i are themselves independent of ordering, the total energy remains unchanged under permutation.

This property reflects the conservative nature of the gravitational field: the binding energy is determined solely by the final mass distribution and not by the path taken to assemble it.

The resulting procedure is therefore characterized by two essential features: (i) additivity, whereby each density class contributes an individual energy term, preserving the transparency of the mass–energy budget; and (ii) permutation invariance, ensuring that the final result is independent of the sequencing of stellar populations and therefore physically consistent.

Together, these properties define an exact, reproducible, and permutation-invariant estimator of effective gravitational binding energy suitable for heterogeneous stellar systems.

3.4 *Energy as a Function of Stellar Fractions*

The effective gravitational binding energy can be written directly as a function of the stellar mass fractions. Let $M = M_{\text{stars}} + M_{\text{gas}}$ be the total baryonic mass of the galaxy and ϕ_i the mass fraction of stellar component i, such that

$$\sum_{i=1}^{n} \phi_i = 1, \qquad M_i = \phi_i M. \tag{7}$$

In the absence of gas clumping ($\kappa = 0$), the gas component is treated as diffusely distributed and is implicitly included in the stellar fraction parametrization.

Let ρ_i denote the intrinsic density of component i. The total effective binding energy then takes the form

$$\Delta E_{\rm tot}(M, \boldsymbol{\phi}) = \frac{3G}{5} M^{5/3} \left[\sum_{i=1}^{n} \left(\frac{4\pi\rho_i}{3} \right)^{1/3} \phi_i^{5/3} + \left(\frac{4\pi}{3} \right)^{1/3} \left(\sum_{i=1}^{n} \frac{\phi_i}{\rho_i} \right)^{-1/3} \right]. \tag{8}$$

This expression depends only on the total baryonic mass and on the set of stellar fractions $\{\phi_i\}$, while the densities ρ_i are fixed properties of the stellar classes.

The effective dark mass associated with this configuration, as discussed previously, is then defined as

$$M_{\rm dark}^{\rm pred} = \frac{\Delta E_{\rm tot}(M, \boldsymbol{\phi})}{c^2}. \tag{9}$$

The reconstruction problem therefore consists in determining the set of fractions $\{\phi_i\}$ that reproduces the observed dark mass for a given galaxy.

An additional degree of freedom can be introduced to account for gas clumping effects. Let $\kappa \in [0, 1]$ denote a gas clumping parameter. The effective mass entering the energy estimate can then be written as

$$M_{\rm eff} = M\,(1 - \kappa). \tag{10}$$

The binding energy can therefore be generalized as

$$\Delta E_{\rm tot}(M_{\rm eff}, \boldsymbol{\phi}). \tag{11}$$

This parameter allows the effective gravitational contribution of the gas component to be modulated, mimicking configurations in which the gas is more or less spatially concentrated than the stellar component.

4. Greedy Reconstruction Algorithm

4.1 *Optimization Problem*

The reconstruction of the stellar population is formulated as a constrained optimization problem over the fraction vector $\boldsymbol{\phi}$. The objective is to minimize the relative error between the predicted dark mass and the observed one:

$$\mathcal{E}(\boldsymbol{\phi}) = \frac{\left| M_{\rm dark}^{\rm pred}(M, \boldsymbol{\phi}) - M_{\rm dark}^{\rm obs} \right|}{M_{\rm dark}^{\rm obs}}. \tag{12}$$

The parameter space is explored using a greedy algorithm based on local linear updates of the fractions. We start with $\lambda = \lambda_{max}$.

4.2 *Local Update Rule*

At each iteration, candidate moves are constructed by perturbing a single component ϕ_i according to

$$\phi_i \to \phi_i + \delta_i, \qquad \delta_i \in \{-\lambda\sigma_i,\ +\lambda\sigma_i\}, \tag{13}$$

where σ_i defines the characteristic variation scale of component i (see Section 4.5), and λ is a dimensionless step-size parameter controlling the amplitude of the update. The updated vector is then renormalized. Configurations violating the bounds are discarded:

$$\sum_{i=1}^{n} \phi_i = 1, \tag{14}$$

$$\max\left(0,\ \phi_i^{(0)} - k\sigma_i\right) \ \le\ \phi_i \ \le\ \min\left(1,\ \phi_i^{(0)} + k\sigma_i\right), \tag{15}$$

where $\phi_i^{(0)}$ denotes the initial fraction of component i, and σ_i defines the characteristic variation scale, with k controlling the allowed deviation.

4.3 *Admissible Moves and Selection Strategies*

Each admissible perturbation defines a candidate configuration $\boldsymbol{\phi}'$, for which the error $\mathcal{E}(\boldsymbol{\phi}')$ is evaluated.

Among all admissible candidates, the subset of improving moves is defined as

$$\mathcal{G} = \left\{ (i, s) \;\middle|\; \mathcal{E}(\boldsymbol{\phi}_{i,s}) < \mathcal{E}(\boldsymbol{\phi}) \right\}, \tag{16}$$

where $\boldsymbol{\phi}_{i,s}$ denotes the configuration obtained by applying a perturbation of sign $s \in \{-1, +1\}$ to component i.

The algorithm proceeds by selecting one admissible move from the set $\mathcal{G}$ and updating the current configuration accordingly:

$$\boldsymbol{\phi} \leftarrow \boldsymbol{\phi}_{i^*, s^*}. \tag{17}$$

Several selection strategies can be defined for choosing the move (i^*, s^*).

(i) Dark-mass greedy selection. The move producing the largest reduction of the dynamical error is selected:

$$(i^*, s^*) = \arg\min_{(i,s)\in\mathcal{G}} \mathcal{E}(\boldsymbol{\phi}_{i,s}). \tag{18}$$

(ii) Photometry-assisted selection. Among the admissible moves, the selected update minimizes a photometric distance $\mathcal{D}_{\rm phot}$ between predicted and reference galaxy colors:

$$(i^*, s^*) = \arg\min_{(i,s)\in\mathcal{G}} \mathcal{D}_{\rm phot}(\boldsymbol{\phi}_{i,s}). \tag{19}$$

(iii) Random selection. A move is selected uniformly at random among the admissible improving moves:

$$(i^*, s^*) \sim \text{Uniform}(\mathcal{G}). \tag{20}$$

4.4 *Multi-Scale Greedy Descent*

This process (as defined in Sections 4.2 – 4.4) is repeated until no further improving move can be found:

$$\mathcal{G} = \varnothing. \tag{21}$$

When no improving move is found at the current variation scale and $\lambda > \lambda_{\min}$, the step-size parameter is reduced according to

$$\lambda \leftarrow \frac{\lambda}{2}. \tag{22}$$

Conversely, when an improving move is found and $\lambda < \lambda_{\max}$, the step size may be increased back toward the coarser exploration scale:

$$\lambda \leftarrow 2\lambda. \tag{23}$$

If no improving move is found and $\lambda \leq \lambda_{\min}$ and gas clumping is enabled, the algorithm then performs a one-dimensional search over the gas clumping parameter $\kappa \in [0, 1]$. At fixed stellar fractions, the selected value is

$$\kappa^* = \arg\min_{\kappa \in [0,1]} \mathcal{E}(\boldsymbol{\phi}, \kappa), \tag{24}$$

where the error function is now evaluated using the effective mass

$$M_{\text{eff}} = M_{\text{bar}}(1 - \kappa). \tag{25}$$

In practice, this minimization is performed by scanning the interval $[0, 1]$ with a fixed resolution $\Delta\kappa = 10^{-3}$. If an improved value κ^* is found, the current configuration is updated,

$$\kappa \leftarrow \kappa^*, \tag{26}$$

and the fraction search is restarted at the maximum step size $\lambda_{\max}$.

The algorithm therefore terminates only when no improving stellar-fraction move exists at $\lambda \leq \lambda_{\min}$, and no further improvement can be obtained by varying κ, if gas clumping is enabled.

In practice, the exploration scale is progressively refined through the step-size parameter λ, which is reduced when no improving move can be found at a given scale. This multi-scale strategy allows the algorithm to explore the parameter space at decreasing resolutions until convergence.

The resulting procedure is fully specified: for fixed initial fractions $\boldsymbol{\phi}$ and bounds on $\boldsymbol{\phi}$ defined by the $\phi_i^{(0)} \pm k\sigma_i$ intervals, the algorithm produces a well-defined solution for any given selection rule within $\mathcal{G}$.

4.5 *Initial Stellar Population and Bounds*

The reconstruction begins from a reference stellar population spanning a wide range of intrinsic densities, from diffuse main-sequence stars to ultra-compact remnants. The components include black holes (BH), neutron stars (NS), white dwarfs (WD), red giants (RG), and the standard spectral classes from O to M. This basis is not intended to reproduce a detailed stellar census; rather, it provides a physically motivated density spectrum capable of generating the gravitational energy required by the dynamical constraints. In particular, the inclusion of compact and high-density components is driven by their contribution to the gravitational binding energy, not by any attempt to optimize the photometric properties of the population.

Each component i is associated with an initial mass fraction $\phi_i^{(0)}$ and a characteristic dispersion σ_i. For nearby galaxies ($z \approx 0$), consistent with the populations represented in SPARC, we adopt the following average fractions normalized to unity:

BH = 1.0% ± 0.5%	NS = 0.3% ± 0.1%
WD = 2.2% ± 0.7%	RG = 0.2% ± 0.1%
M = 55% ± 10%	K = 16% ± 6%
G = 10.5% ± 5%	F = 5.5% ± 3%
A = 5% ± 2%	B = 3% ± 1%
O = 1.3% ± 0.5%	

These values define the initial fraction vector $\boldsymbol{\phi}^{(0)}$ and the associated dispersion scales $\{\sigma_i\}$ used in the reconstruction.

The exploration of the parameter space is constrained by bounding each fraction within a fixed interval around its initial value:

$$\max\left(0,\, \phi_i^{(0)} - k\sigma_i\right) \;\leq\; \phi_i \;\leq\; \min\left(1,\, \phi_i^{(0)} + k\sigma_i\right), \tag{27}$$

where k is a global parameter controlling the allowed deviation from the reference population. In all subsequent analyses, we adopt $k = 3$.

These bounds define the admissible region of the parameter space and ensure that the reconstructed populations remain within physically plausible variations of the initial stellar mixture.

4.6 *Random Initialization of the Stellar Fractions*

In addition to the reference initial population $\boldsymbol{\phi}^{(0)}$, alternative initial configurations can be generated by sampling the stellar fractions within their admissible bounds.

For each component i, a temporary fraction is drawn uniformly within the allowed interval:

$$\tilde{\phi}_i \sim \mathcal{U}\Big[\max\left(0,\, \phi_i^{(0)} - k\sigma_i\right),\; \min\left(1,\, \phi_i^{(0)} + k\sigma_i\right)\Big], \tag{28}$$

where $\mathcal{U}$ denotes the uniform distribution. The updated vector is then renormalized to satisfy

$$\phi_i = \tilde{\phi}_i \,/\, \sum_{j=1}^{n} \tilde{\phi}_j, \tag{29}$$

and retained only if it satisfies the bounds

$$\max\left(0,\, \phi_i^{(0)} - k\sigma_i\right) \;\le\; \phi_i \;\le\; \min\left(1,\, \phi_i^{(0)} + k\sigma_i\right), \tag{30}$$

where $\phi_i^{(0)}$ denotes the initial fraction of component i, and $k\sigma_i$ defines the allowed variation scale.

This procedure is repeated until a valid normalized configuration is obtained.

The components are sampled in random order to avoid introducing any systematic bias in the construction of the initial vector.

This randomized initialization provides alternative starting points within the admissible parameter space and allows the sensitivity of the reconstruction to initial conditions to be assessed.

5. Controlled Experiments and Robustness Tests

5.1 *No-Search Baseline*

In order to assess whether the observed correlations could arise trivially from the choice of initial stellar fractions, we perform a baseline test in which no optimization is applied.

In this configuration, the stellar fractions are used directly, without any greedy search or iterative adjustment, and gas clumping is disabled ($\kappa = 0$). The predicted dark mass and photometric quantities are therefore computed from the initial population only.

Two types of initial configurations are considered:

(i) Reference initialization. The fixed initial population $\boldsymbol{\phi}^{(0)}$ is used.

(ii) Random initialization. The stellar fractions are randomly sampled within the admissible bounds, as described in Section 4.6.

The reconstruction performance obtained under these conditions is summarized in Table 1. In both cases, only a small fraction of galaxies are successfully reconstructed, and the mean relative error remains large.

More importantly, no significant correlation is observed between predicted and observed photometric properties. Both random and reference initializations yield Pearson and Spearman coefficients consistent with weak or marginal correlations across all color indices.

The corresponding photometric correlations are reported in Table 2. The random initialization yields coefficients close to zero in all cases, while the reference initialization shows slightly larger amplitudes, with several values approaching 1σ and a peak at 2σ for the Pearson coefficient of NUV–r. This suggests that the reference initialization performs marginally better, although the correlations remain weak and statistically inconclusive overall.

Table 1. Reconstruction performance without optimization.

	Random	**Reference**
Galaxies Solved	27	22
Success Rate	15.5%	12.6%
Mean Rel. Error	20.98	19.19
Std Dev	46.98	35.49

Table 2. Correlation analysis without optimization.

	N	$r_{\rm P}$	$\sigma_{\rm P}$	$\rho_{\rm S}$	$\sigma_{\rm S}$
Random initialization					
FUV–NUV	136	-0.006	0.07	0.014	0.16
$r-z$	129	-0.004	0.04	-0.049	0.56
$g-r$	128	0.077	0.87	0.053	0.60
NUV–r	119	0.036	0.39	0.041	0.44
Reference initialization					
FUV–NUV	136	0.091	1.05	0.072	0.83
$r-z$	129	0.110	1.24	0.076	0.86
$g-r$	128	-0.092	1.04	-0.073	0.82
NUV–r	119	-0.184	2.00	-0.135	1.47

These results show that, in the absence of any optimization, the reconstruction does not reliably reproduce the observed dynamical constraints, with large relative errors and a low fraction of successfully fitted galaxies. It also does not recover the observed photometric correlations.

Instead, they emerge only when the dynamical constraint is actively enforced through the reconstruction procedure. This confirms that neither the allowed parameter space, nor the reference initialization, nor the intrinsic model structure alone is sufficient to produce correlations in the absence of an active reconstruction procedure.

This also indicates that the correlations are not the result of a passive mapping between mass and photometric properties, but require an explicit enforcement of the dynamical constraint to emerge. In this sense, the reconstruction procedure does not simply reveal a pre-existing relation, but actively selects configurations that are consistent with both the dynamical and photometric ordering.

5.2 *Effect of the Search Strategy*

We now compare three search strategies applied to the same reconstruction problem: (i) a random choice among the improving dark-mass moves, (ii) a photometry-assisted choice, and (iii) a simple greedy selection based only on the dark-mass error. For each strategy, we consider both reference and random initial fractions. In all cases, the reconstruction is performed using only the outermost kinematic point of each galaxy and with no gas clumping.

Table 3 summarizes the dynamical reconstruction performance. All configurations yield very similar results, with approximately two thirds of the galaxies successfully reconstructed. The success rate remains in a narrow range between 66% and 68%, with comparable mean relative errors and standard deviations across all strategies and initializations.

Table 3. Reconstruction performance for different search strategies using only the outermost kinematic point of each galaxy and with no gas clumping.

	Random	**Reference**
Random DM step		
Galaxies Solved	118	118
Success Rate	67.8%	67.8%
Mean Rel. Error	1.170	1.153
Std Dev	2.763	2.714
Photometry-assisted		
Galaxies Solved	115	115
Success Rate	66.1%	66.1%
Mean Rel. Error	1.284	1.328
Std Dev	3.018	3.246
Simple DM greedy		
Galaxies Solved	119	119
Success Rate	68.4%	68.4%
Mean Rel. Error	1.151	1.129
Std Dev	2.719	2.679

The corresponding photometric correlations are reported in Tables 4 and 5, for the random and reference initializations, respectively. Three main trends emerge from the comparison.

First, for a given search strategy, the random initialization systematically leads to weaker correlations than the reference stellar population. This indicates that the proximity of the initial population to physically relevant configurations plays an important role in the reconstruction outcome.

Second, when starting from a random initialization, significant and robust correlations are recovered only when the search is assisted by photometric information. In the absence of such guidance, both the random-choice and simple greedy strategies fail to produce strong or consistent photometric relations, with only moderate or scattered signals that remain significantly weaker and less coherent than in the photometry-assisted case.

Third, the simple dark-mass greedy strategy yields the strongest correlations overall, exceeding those obtained with the photometry-assisted approach when combined with the reference initialization. This result is non-trivial, as the optimization in this case is driven solely by the dark-mass constraint, without any direct photometric input.

Taken together, these results show that the emergence of photometric correlations depends on both the initial conditions and the structure of the search process. While photometric assistance is necessary to recover meaningful results from random initial populations, the most coherent and statistically significant relations are obtained when the optimization follows a systematic descent in the dark-mass error starting from a physically motivated reference population.

This behavior indicates that the dark-mass reconstruction alone can implicitly guide the system toward stellar population mixtures with meaningful photometric ordering. It also shows that the photometric properties are not merely imposed by construction, but can emerge as a consequence of the dynamical optimization. The search trajectory therefore plays a decisive role, not only in achieving convergence, but also in selecting physically relevant solutions.

5.3 *Impact of Gas Clumping*

We now investigate the impact of gas clumping on the reconstruction. The fixed initial population $\boldsymbol{\phi}^{(0)}$ is used, together with the simple greedy dark-mass selection rule described in the previous section, except that gas clumping is enabled. The reconstruction is still performed using only the outermost kinematic point of each galaxy.

In this configuration, the gas clumping parameter κ is treated as an additional degree of freedom and is allowed to vary within the interval $[0, 1]$. When no improving move is found in the stellar-fraction space, the algorithm performs a one-dimensional scan over κ and selects the value that minimizes the relative error. The search is performed with a fixed resolution $\Delta\kappa = 10^{-3}$.

The resulting performance is summarized in Table 6. The inclusion of gas clumping leads to a significant improvement of the dynamical reconstruc-

Table 4. Correlation analysis (Random initialization) using only the outermost kinematic point and no gas clumping.

	N	r_P	σ_P	ρ_S	σ_S
Random DM step					
FUV–NUV	136	-0.164	1.91	-0.097	1.12
$r-z$	129	0.226	2.58	0.199	2.26
$g-r$	128	0.320	3.68	0.253	2.89
NUV–r	119	0.187	2.04	0.203	2.21
Photometry-assisted					
FUV–NUV	136	0.145	1.68	0.208	2.43
$r-z$	129	0.225	2.56	0.294	3.38
$g-r$	128	0.535	6.51	0.605	7.56
NUV–r	119	0.509	5.91	0.590	7.06
Simple DM greedy					
FUV–NUV	136	0.120	1.40	0.138	1.60
$r-z$	129	0.150	1.69	0.029	0.32
$g-r$	128	0.230	2.62	0.173	1.96
NUV–r	119	0.207	2.26	0.258	2.83

Table 5. Correlation analysis (Reference initialization) using only the outermost kinematic point and no gas clumping.

	N	r_P	σ_P	ρ_S	σ_S
Random DM step					
FUV–NUV	136	-0.187	2.18	-0.250	2.93
$r-z$	129	0.072	0.81	0.321	3.71
$g-r$	128	0.326	3.76	0.402	4.71
NUV–r	119	0.331	3.68	0.335	3.73
Photometry-assisted					
FUV–NUV	136	0.146	1.69	0.200	2.34
$r-z$	129	0.185	2.10	0.317	3.67
$g-r$	128	0.545	6.64	0.633	8.01
NUV–r	119	0.551	6.49	0.651	8.02
Simple DM greedy					
FUV–NUV	136	-0.214	2.50	-0.218	2.56
$r-z$	129	0.395	4.63	0.460	5.49
$g-r$	128	0.671	8.67	0.628	7.93
NUV–r	119	0.681	8.51	0.659	8.14

tion. Nearly all galaxies are successfully fitted, and the mean relative error is reduced by more than an order of magnitude.

This improvement is not uniform across the sample. As shown by the internal statistics, gas clumping is selected by the algorithm in a subset of galaxies (59 out of 174), with a mean clumping factor of ~ 0.45. These galaxies correspond to systems where the diffuse gas distribution leads to an overestimation of the gravitational energy, and therefore of the inferred dark mass. Introducing gas clumping reduces the effective contribution of the gas component, bringing the predicted dark mass into agreement with the observations.

Several important trends emerge from these results. First, the clumping factor remains within physically reasonable bounds across the entire sample of kinematic points. Although the algorithm allows the parameter to vary across the full interval $[0, 1]$, no reconstructed configuration produces values below approximately 2.4% or above 81%. Second, the galaxies that require gas clumping are precisely those with the lowest gas fractions. Their median gas fraction is approximately 21%, compared to about 74% for galaxies that do not require clumping. This behavior is physically expected: when the gas mass is small relative to the stellar component, a more concentrated distribution of the gas can significantly modify the gravitational binding energy.

These results show that gas clumping plays an important role in the reconstruction. Without clumping, the model struggles to reproduce the observed dark mass, leading to a large fraction of unsuccessful fits and high relative errors. When clumping is included, the dynamical reconstruction improves significantly, with nearly all galaxies being successfully fitted and a substantial reduction in the relative error.

Table 6. Impact of gas clumping on reconstruction performance for the reference initialization using a simple dark-mass greedy search.

	Without clumping	**With clumping**
Galaxies Solved	119	170
Success Rate	68.4%	97.7%
Mean Rel. Error	1.130	0.028
Std Dev	2.679	0.129

The corresponding photometric correlations are reported in Table 7. The inclusion of gas clumping has only a limited impact on the Pearson correlation coefficients, which remain nearly unchanged across all color indices.

However, a systematic increase in the Spearman rank correlation is observed, with higher significance levels obtained when clumping is enabled. This indicates that gas clumping enhances the monotonic ordering between predicted and observed quantities, even though it does not significantly modify the linear

Table 7. Comparison of photometric correlations with and without gas clumping for the reference initialization using a simple dark-mass greedy search.

	N	r_P	σ_P	ρ_S	σ_S
Without clumping					
FUV–NUV	136	-0.214	2.50	-0.218	2.56
$r-z$	129	0.395	4.63	0.460	5.49
$g-r$	128	0.671	8.67	0.628	7.93
NUV–r	119	0.681	8.52	0.659	8.15
With clumping					
FUV–NUV	136	-0.214	2.50	-0.203	2.37
$r-z$	129	0.395	4.63	0.493	5.93
$g-r$	128	0.670	8.66	0.655	8.40
NUV–r	119	0.682	8.53	0.701	8.87

correlation strength.

This result suggests that gas clumping improves the internal consistency of the reconstruction by reinforcing the rank ordering of stellar populations, while the overall correlation structure remains primarily determined by the optimization process and the underlying model.

5.4 *Full Radial Reconstruction and Point Selection*

In the previous sections, the analysis was restricted to the outermost kinematic point of each galaxy, in order to provide a simple and controlled framework. We now extend the reconstruction to all available kinematic points.

For each galaxy, the reconstruction is performed independently at every radius, using the same algorithmic configuration as in the previous section, including gas clumping. Among all reconstructed points, the solution with the smallest relative error is selected as representative of the galaxy.

This procedure allows us to test whether the results obtained using only the outermost point are robust when considering the full radial structure.

The global statistics, summarized in Table 8, show that the reconstruction remains highly successful. Out of 3048 fitted points, 2983 are reconstructed within the observational uncertainties, corresponding to a success rate of 97.9%.

A point is considered successfully reconstructed if the inferred gravitational energy is consistent with the dynamically inferred dark mass within the observational uncertainties. At the galaxy level, a system is considered successfully reconstructed only if all its kinematic points satisfy this criterion. Under this definition, 149 out of 174 systems are successfully reconstructed (85.6%), with a mean relative error of 0.028 and a standard deviation of 0.129.

The behavior of the gas clumping parameter is consistent with the previous analysis. Clumping is selected in a subset of galaxies (60 out of 174), with a mean value of ~ 0.62.

As in the previous case, clumping occurs preferentially in systems with relatively low gas fractions, while galaxies with high gas fractions typically do not require clumping. The introduction of clumping leads to a very small residual error, indicating that it acts as a fine adjustment of the mass distribution rather than a dominant contribution. This behavior suggests that clumping compensates for specific configurations of the gas component, improving the local consistency of the reconstruction without altering the overall correlation structure.

Table 8. Reconstruction performance using all kinematic points.

Points Solved	**Galaxies Solved**
2983/3048 (97.9%)	149/174 (85.6%)
Mean Rel. Error (selected points)	**Std Dev (selected points)**
0.028	0.129

Importantly, the reconstruction performed over all radial points does not significantly degrade the global dynamical performance of the model. The high success rate and low residual errors indicate that consistent solutions can be found across different radii.

However, the present analysis does not explicitly quantify the internal consistency of the reconstructed solutions within each galaxy. In addition, the radial distribution of the selected best-fit points is broad, with a mean normalized position of ~ 0.44 and a standard deviation of ~ 0.27, spanning the full radial range from the inner to the outer regions. The median value ~ 0.44 confirms that the distribution is approximately centered within the disk. Nevertheless, the stability of the global statistics suggests that the results obtained using only the outermost point are not dominated by a specific radial selection.

The photometric correlations, reported in Table 9, remain strong and statistically significant across multiple color indices, confirming the robustness of the results with respect to the radial sampling. However, their distribution differs from the outermost-point case (Table 7). In particular, the UV correlation (FUV–NUV) is significantly enhanced, while the correlations in $r-z$, $g-r$ and NUV–r are reduced compared to their peak values obtained with the outermost point.

Table 9. Photometric correlations using all kinematic points.

	N	r_P	σ_P	ρ_S	σ_S
FUV–NUV	136	-0.319	3.79	-0.388	4.67
$r-z$	129	0.280	3.22	0.355	4.12
$g-r$	128	0.585	7.25	0.573	7.07
NUV–r	119	0.587	7.02	0.588	7.04

This difference likely reflects a shift in the radial location of the selected best-fit point when all kinematic radii are considered. In particular, the retained solution lies at smaller radii in some galaxies; the corresponding reconstructed population may contain a larger contribution from younger stars, which could preferentially affect UV-sensitive colors such as FUV–NUV.

Overall, this analysis shows that the conclusions drawn from the simplified one-point reconstruction extend to the full set of kinematic data, supporting the validity of the method at the galaxy scale.

5.5 *Stellar Population Composition in Galaxy Types*

We consider a representative subset of galaxies spanning a range of morphological types, from gas-rich irregular systems to more structured spiral disks. The sample includes DDO154 (Im) and NGC4214 (Im), both characterized by irregular morphologies and significant gas content; NGC2403 (Scd), NGC6503 (Scd), and NGC4183 (Scd), which are late-type disk galaxies with well-defined rotational structures; F568-3 (Sd), NGC0247 (Sd), and NGC0300 (Sd), representing diffuse and extended stellar disks; F568-1 (Sc), an intermediate spiral; and NGC3769 (Sb), corresponding to an earlier-type spiral with a more prominent stellar component.

The stellar population fractions shown in Figure 1 are derived directly from the reconstruction algorithm by evaluating only the last point of the galaxy on which a greedy optimization is performed on the dark mass component. The result corresponds to normalized contributions of stellar remnants (BH, NS, WD, RG) and main-sequence spectral classes (M, K, G, F, A, B, O). No adjustments or smoothing have been applied to these outputs.

The selected galaxies are not intended to be exhaustive but rather to illustrate typical behaviors across morphological classes. Cases where the reconstruction converges toward extreme or boundary solutions are deliberately excluded, as they reflect specific configurations of the model rather than generic population trends.

A qualitative trend is observed across the sequence: late-type and irregular galaxies are dominated by low-mass stars (M and K types), while earlier-type spirals tend to exhibit a higher contribution from intermediate-mass stellar populations (G, F, and A). Stellar remnants remain subdominant across all systems, although non-negligible.

These trends should be interpreted with caution. While the reconstructed populations exhibit a coherent progression across morphological types, this behavior remains qualitative and does not constitute a statistical validation of the model. In particular, although the dominance of low-mass stars in late-type systems and the increasing contribution of intermediate-mass stars toward earlier-type spirals are consistent with expectations from stellar population synthesis, these results remain dependent on the reconstruction procedure.

The reconstruction also admits extreme or degenerate solutions in certain regions of parameter space. Such cases are not shown here, as they do not reflect typical galaxy properties. A systematic exploration of these regimes is left for future work.

More importantly, the emergence of physically plausible stellar populations appears to be a robust feature of the reconstruction process itself. Within the greedy optimization procedure, solutions corresponding to realistic population mixes appear to act as attractors in the parameter space, toward which the algorithm converges without explicit constraints enforcing astrophysical plausibility. This convergence toward realistic configurations suggests that the mapping between gravitational binding energy and stellar population fractions is unlikely to be arbitrary, but instead reflects underlying structural constraints imposed by the dynamics, linking the mass–energy distribution to the internal composition of galaxies.

This behavior is non-trivial. The reconstruction is driven solely by the evaluation of gravitational potential energy and its mapping to an effective mass component, with no prior requirement that the resulting stellar populations be astrophysically realistic. In particular, there is no a priori reason for such a framework to simultaneously reproduce dark matter phenomenology and yield credible stellar population distributions.

The spontaneous convergence toward physically meaningful populations therefore provides additional support for the internal coherence of the model, suggesting that the underlying mechanism captures some relevant structural features of galactic systems, even though a full statistical validation remains to be established.

This approach relies on the last kinematic point of each galaxy, which typically probes the outer regions where the balance between baryonic and effective dark components is established and where dark mass contributions become dominant.

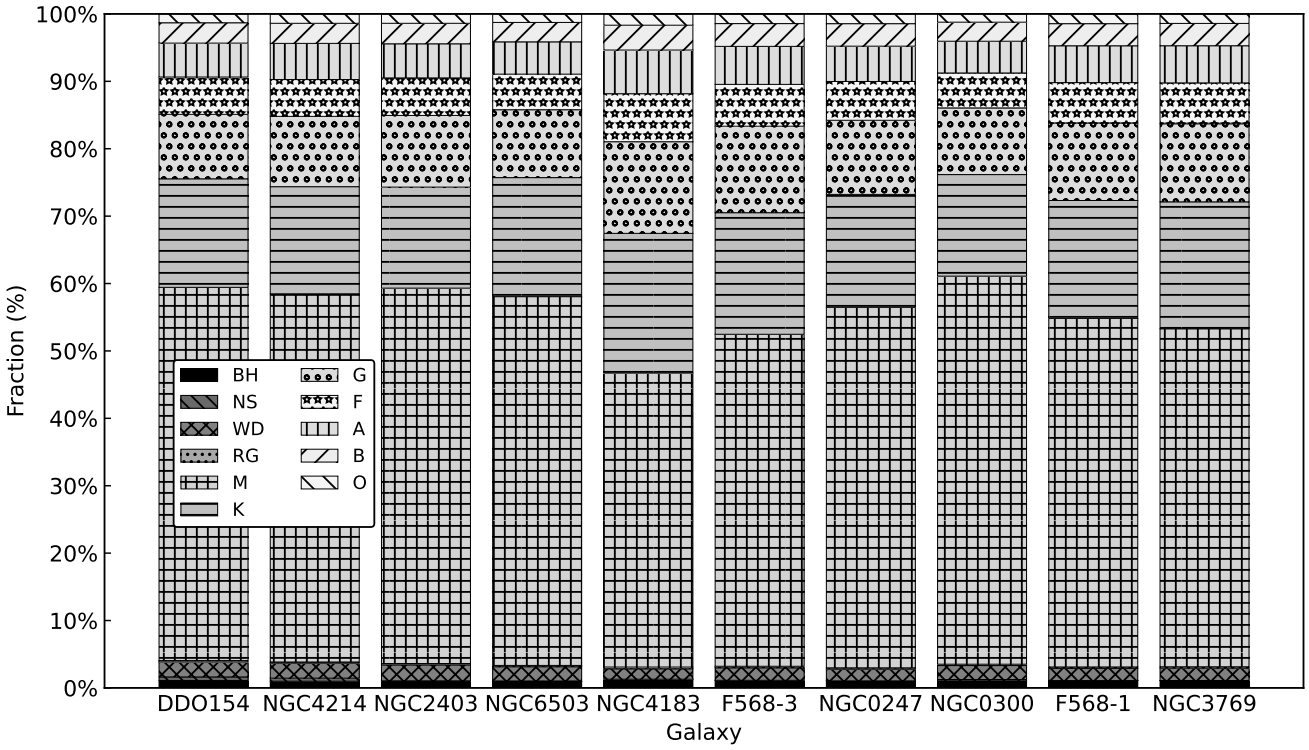

Figure 1. Stellar population fractions for a representative sample of galaxies spanning morphological types from irregular (Im) to early-type spirals (Sb). The fractions correspond to stellar remnants (BH, NS, WD, RG) and main-sequence spectral classes (M to O), derived directly from the reconstruction algorithm.

6. Statistical Comparison and Robustness Tests

Up to this point, we have established several key results regarding the reconstruction of stellar populations from galactic dynamics.

First, the no-search baseline (Section 5.1) demonstrated that the initial stellar fractions and their admissible bounds alone do not produce any significant photometric correlations. In the absence of optimization, both Pearson and Spearman coefficients remain consistent with weak or marginal signals, showing that the correlations are not trivially encoded in the initial conditions or in the structure of the parameter space.

Second, the comparison of search strategies (Section 5.2) showed that the reconstruction of the dark mass component is not sufficient by itself to ensure photometric agreement. While multiple strategies can reproduce the dynamical constraints with comparable accuracy, only specific reconstruction paths lead to strong and consistent photometric correlations. In particular, a systematic greedy descent driven by the dark-mass constraint yields the most robust ordering relations when starting from a physically motivated reference population.

Third, the introduction of gas clumping (Section 5.3) demonstrated that the dynamical reconstruction can be significantly improved without altering the overall structure of the correlations. The inclusion of this additional degree of freedom leads to a substantial reduction in the relative error while preserving, and in some cases enhancing, the rank-order relations between predicted and observed quantities.

Fourth, the full radial reconstruction (Section 5.4) showed that the emergence of photometric correlations is not restricted to a specific radial selection. Consistent solutions are obtained across different kinematic points, indicating that the ordering relations are a stable feature of the reconstruction process at the galaxy scale.

In addition, the analysis of reconstructed stellar populations across galaxy types (Section 5.5) showed that the resulting population mixtures are unlikely to be arbitrary, but exhibit coherent and physically plausible trends. In particular, late-type and irregular galaxies are dominated by low-mass stars, while earlier-type spirals display an increased contribution from intermediate-mass stellar populations. This qualitative behavior emerges without any explicit astrophysical prior on the stellar content.

Taken together, these results show that dynamically reconstructed stellar populations reproduce statistically

significant photometric correlations without using any photometric information, and that these correlations are not trivially imposed by the initial conditions or by the structure of the model.

However, such correlations could in principle arise from statistical fluctuations, implicit selection effects, or observational systematics.

The purpose of this section is therefore to assess the statistical robustness and physical origin of the observed relations.

All results presented in the following analysis are obtained using the simple greedy reconstruction driven by the dark mass constraint, evaluated at the outermost radial point of each galaxy, and including the gas clumping correction (see Tables 6 and 7).

6.1 *Mass-Driven Origin of the Photometric Ordering*

The reconstruction associates a stellar population to each pair $(M_{\rm bar}, M_{dark})$, which is then mapped to photometric properties. However, in the SPARC sample, the inferred dark mass is found to be very strongly correlated with the baryonic mass ($\rho \approx 0.95$), indicating that the two quantities are not independent.

As a result, the space of admissible pairs $(M_{\rm bar}, M_{dark})$ is effectively confined to a narrow one-dimensional locus. Variations of M_{dark} at fixed $M_{\rm bar}$ are strongly limited, and do not span an independent degree of freedom.

This implies that the reconstruction effectively operates on a one-dimensional manifold, where both $M_{\rm bar}$ and M_{dark} are controlled by the same underlying scaling. Consequently, the photometric ordering is primarily driven by this global mass dependence, rather than by independent variations of the dark mass component.

This interpretation is directly confirmed by the empirical correlations measured across the sample. For the optical and UV-optical colors ($g - r$, $r - z$, and NUV$-r$), the observed photometric ranking is found to be strongly correlated with both baryonic mass and inferred dark mass, with Spearman coefficients in the range $\rho \sim 0.54$–0.76, corresponding to significances between $\sim 6\sigma$ and $\sim 10\sigma$.

However, no significant correlation is detected with the ratio $M_{dark}/M_{\rm bar}$, indicating that relative variations between baryonic and dark components do not control the ordering. This is consistent with the absence of an independent degree of freedom in M_{dark}.

Furthermore, the correlations obtained from the reconstructed populations do not exceed those obtained using baryonic mass alone. This shows that the reconstruction does not introduce additional ordering beyond that already encoded in the global mass scaling, but rather recovers it through the dynamical constraints.

Taken together, these results provide empirical support for the conclusion that the photometric ordering is primarily mass-driven.

Although this result does not reveal new information about the well-known relation between galaxy mass and photometry, it does not contradict the central claim that dynamical constraints encode information relevant to photometric properties.

In the present framework, the reconstruction maps a pair $(M_{\rm bar}, M_{dark})$ to a stellar population, which in turn determines the photometric properties. This mapping is obtained without using any photometric information, and relies only on baryonic mass and the dynamically inferred dark mass. It is defined by an explicit, computable function derived from the underlying physical construction of the model, rather than by any empirical mapping or lookup relation.

What is new is therefore not the existence of a mass–photometry correlation itself, but the fact that such a relation can be recovered through a calculable transformation based solely on dynamical quantities.

Furthermore, the strong correlation observed between $M_{\rm bar}$ and M_{dark} in the present sample implies that the explored parameter space is effectively one-dimensional. This does not exclude the possibility that a broader galaxy sample, sampling more uniformly the $(M_{\rm bar}, M_{dark})$ space, could reveal additional structure and potentially disentangle independent contributions from baryonic and dark components. Exploring this possibility would require a significantly larger and more diverse dataset, and remains an open question.

An additional aspect of particular interest for astrophysical applications is that dynamical constraints can be obtained across the full radial extent of galaxies, whereas photometric information is often more limited in radial coverage, signal-to-noise, or interpretability in terms of stellar populations.

In this context, the present reconstruction provides a calculable relation that can be applied at all radii, allowing one to infer the underlying stellar population structure from dynamical quantities alone. This offers a complementary approach to photometric analyses, with the potential to probe radial variations of stellar populations in regimes where direct photometric constraints are incomplete or uncertain.

6.2 *Monotonic Structure of the Correlations*

To further characterize the nature of the observed correlations, we examine their structure in rank space. This allows us to test whether the relations between predicted and observed photometric quantities are consistent with a simple monotonic ordering.

For each observable, we consider the relation between the predicted and observed ranks and perform a linear fit of the form $r_y = a\, r_x + b$. This representa-

tion is not intended to capture the detailed physical relation, but rather to provide a minimal description of the global ordering. The rank–rank distributions are shown in Figs. 2–5, and the corresponding fit parameters are summarized in Table 10.

Table 10. Linear fits in rank space ($r_y = a\, r_x + b$).

	N	a	b
FUV–NUV	136	81.17 ± 6.61	−0.203 ± 0.085
$r - z$	129	32.48 ± 5.72	0.493 ± 0.077
$g - r$	128	21.88 ± 4.94	0.655 ± 0.067
NUV–r	119	17.66 ± 4.50	0.701 ± 0.066

For the optical and UV-optical colors ($g - r$, $r - z$, and NUV−r), the distributions exhibit a clear monotonic trend, with points aligned along a well-defined diagonal. The corresponding linear fits are consistent with positive slopes of order unity, indicating that the reconstruction preserves the global ordering of galaxies across these observables.

In contrast, the UV color FUV−NUV exhibits a more complex structure in rank space. While the distribution is not random, it does not follow a single monotonic relation, but instead suggests the presence of multiple regimes. This behavior is consistent with the weaker correlations identified in the previous sections and suggests that additional physical processes, such as recent star formation, contribute to shaping this observable.

Overall, the rank-space analysis supports the conclusion that the reconstructed populations reproduce a coherent monotonic ordering for most photometric quantities, while also revealing departures from this simple behavior in the ultraviolet regime.

6.3 *Bootstrap and Jackknife*

We now assess whether the observed correlations could arise from statistical fluctuations or sampling effects. To this end, we perform jackknife (Quenouille, 1949; Tukey, 1958) and bootstrap (Efron & Tibshirani, 1993) resampling tests on the galaxy sample.

In the bootstrap analysis, we generate 10^6 realizations of the dataset by sampling galaxies with replacement and recompute the correlation coefficients for each realization. The resulting distributions are well converged and show narrow confidence intervals. In particular, for the optical and UV-optical colors ($g - r$, $r-z$, and NUV−r), no sign changes are observed across all realizations, indicating a stable and well-defined ordering.

In the jackknife analysis, we systematically remove one galaxy at a time and recompute the correlations. The resulting standard errors are small, indicating that the correlations are not driven by any individual galaxy.

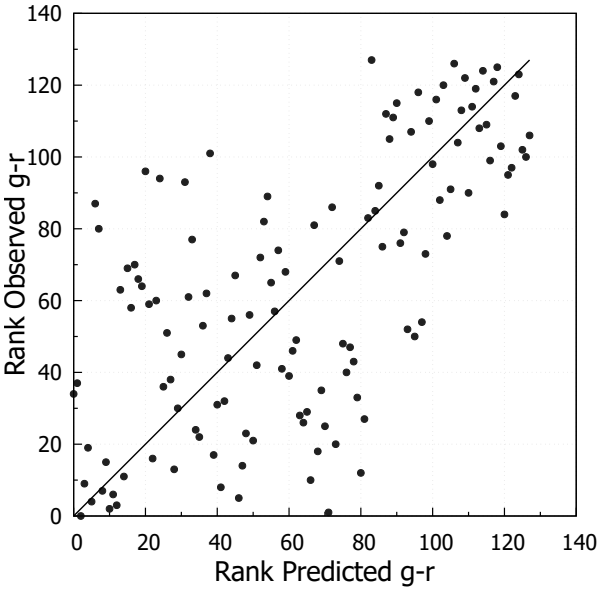

Figure 2. Rank–rank comparison between predicted and observed $g - r$ color.

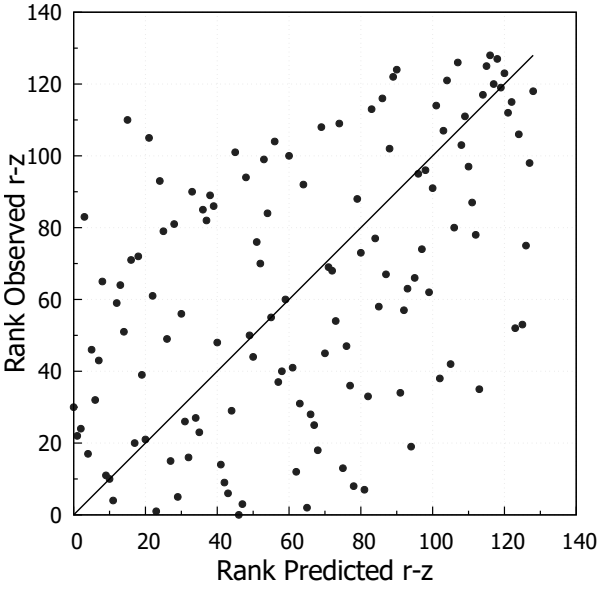

Figure 3. Rank–rank comparison between predicted and observed $r - z$ color.

In contrast, the FUV–NUV correlation exhibits a larger dispersion under resampling, with a small but non-zero fraction of sign changes. This indicates that the corresponding relation is weaker and more sensitive to sampling, consistent with the more complex structure observed in rank space.

Overall, these tests show that the main correlations are statistically robust and not driven by sampling ef-

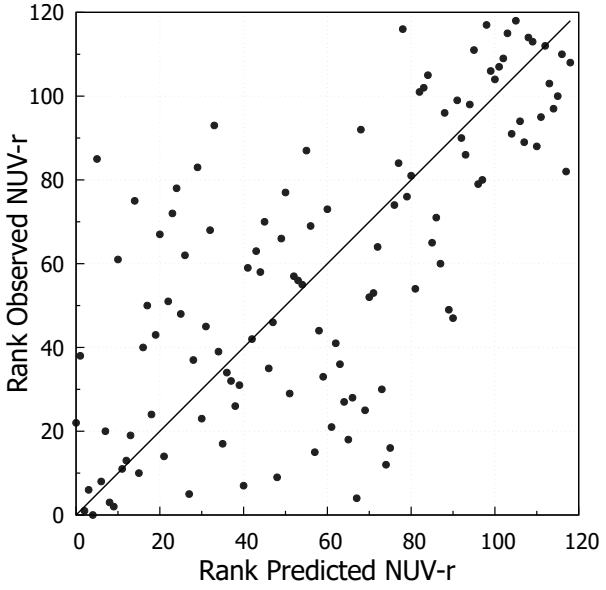

Figure 4. Rank–rank comparison between predicted and observed NUV − r color.

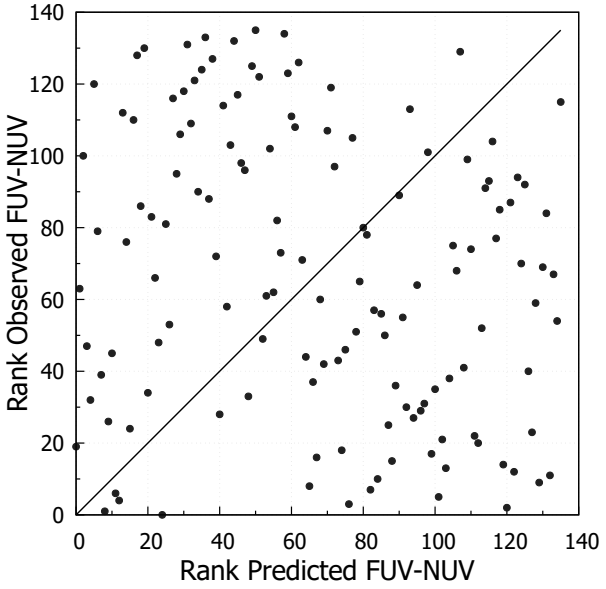

Figure 5. Rank–rank comparison between predicted and observed FUV − NUV color.

fects and are robust to resampling, while the ultraviolet regime displays intrinsically weaker and variable behavior. The agreement between bootstrap and jackknife estimates further indicates that the inferred correlations are not sensitive to the resampling procedure, and that the observed signal is consistently recovered across independent resampling strategies.

The bootstrap confidence intervals and jackknife uncertainties are summarized in Table 11.

Table 11. Bootstrap (10^6 realizations) and jackknife robustness tests based on Spearman correlations. Flip denotes the fraction of bootstrap realizations with a change of sign.

	ρ	**16/84%**	**Flip**	**JK SE**
FUV–NUV	-0.20	[-0.29, -0.12]	0.01	0.086
$r-z$	0.49	[0.42, 0.56]	0	0.067
$g-r$	0.65	[0.59, 0.71]	0	0.056
NUV–r	0.70	[0.64, 0.75]	0	0.055

6.4 *Permutation Tests*

In addition, non-parametric permutation tests (Good, 2005) are used to assess the statistical significance of the observed correlations. For each observable, 10^8 random permutations of the photometric data are generated to construct the null distribution, corresponding to the distribution of correlation coefficients obtained under the hypothesis of no intrinsic association.

The resulting p-values are converted into Gaussian-equivalent significance levels using the two-sided relation to the standard normal distribution. All significance levels quoted in the following sections are expressed as Gaussian-equivalent sigma.

For the optical and UV-optical colors ($g-r$, $r-z$, and NUV$-r$), the resulting p-values are at or below 10^{-8}, corresponding to significance levels of $\gtrsim 5.7\sigma$, indicating that the observed correlations are highly unlikely to arise from random associations. In contrast, the FUV–NUV correlation yields p-values of order 10^{-2}, corresponding to a significance of $\sim 2.4\sigma$, consistent with its weaker and more variable behavior.

These results provide an independent, non-parametric assessment of the statistical significance of the main correlations.

6.5 *Inclination Systematics*

A potential concern in the interpretation of photometric correlations is the role of galaxy inclination, which can affect observed colors through dust attenuation, projection effects, and internal extinction. To assess whether the ordering relations identified above are driven by such systematics, we explicitly examine the dependence of the correlations on the inclination angle. The robustness of the results is evaluated using bootstrap resampling (10^6 realizations) and non-parametric permutation tests (10^8 realizations).

Figures 6 and 7 display the rank–rank relations for the $g-r$ and NUV–r colors, with each galaxy encoded by its inclination angle in grayscale. No segregation of points along the inclination axis is observed that could account for the global monotonic trends. In particular, galaxies with similar predicted ranks span a wide range of inclinations, indicating that the primary ordering is

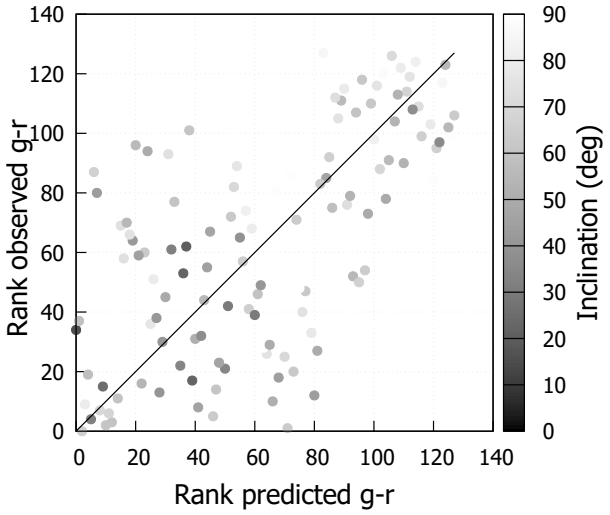

Figure 6. Rank–rank comparison between predicted and observed $g - r$ color. The gray level encodes galaxy inclination from face-on (dark) to edge-on (light).

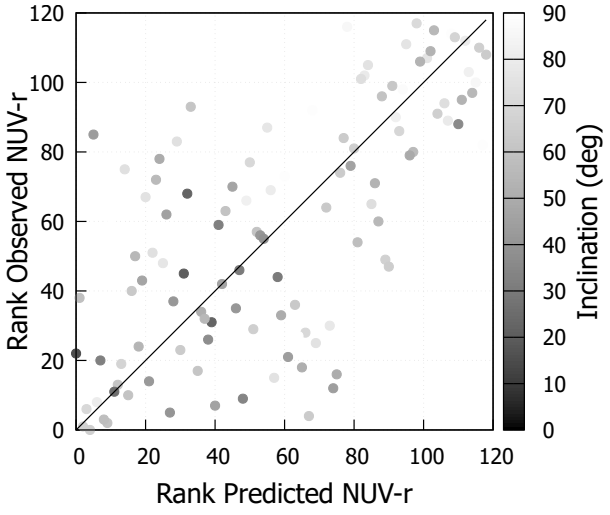

Figure 7. Rank–rank comparison between predicted and observed NUV $- r$ color. The gray level encodes galaxy inclination from face-on (dark) to edge-on (light).

not trivially set by viewing geometry. The $r - z$ color shows a similar behavior, while the FUV–NUV relation remains weak and more dispersed across all inclination ranges.

This conclusion is reinforced by direct correlation tests between inclination and the color residuals. For all four color indices, both Pearson and Spearman coefficients between the residuals and inclination remain significantly weaker than the main predicted–observed correlations. However, moderate correlations are detected, with typical amplitudes $|\rho| \sim 0.25$–0.35 and statistical significances at the ~ 3–4σ level, especially in the ultraviolet and UV–optical bands. These correlations are nonetheless insufficient to reproduce the observed rank–rank relations or to account for their strength.

Additional insight is obtained by splitting the sample into low-, mid-, and high-inclination subsamples. In the low-inclination regime ($i < 45°$), the correlations are weak and statistically insignificant, with large dispersion under resampling. In contrast, intermediate and high inclinations ($45° \leq i < 70°$ and $i \geq 70°$) exhibit clear and statistically significant monotonic relations. For the optical and UV–optical colors ($g - r$ and NUV–r), permutation tests yield p-values as low as $\sim 10^{-8}$, corresponding to significance levels of $\gtrsim 5.7\sigma$, while the $r - z$ relation remains significant at the ~ 4.7–5.7σ level depending on the estimator.

The purely ultraviolet FUV–NUV color displays a more complex behavior. No statistically significant correlation is detected at low inclinations, and only weak signals are present at intermediate and high inclinations, consistent with its intrinsically more variable nature.

Taken together, these results show that inclination effects do not appear to generate the observed ordering relations. Instead, inclination primarily modulates their observational detectability, with the underlying correlations becoming more clearly visible in systems with stronger projected gradients. The dominant signal therefore is consistent with an intrinsic connection between the dynamically inferred stellar populations and the global photometric properties of galaxies, rather than a projection-induced bias.

6.6 *Morphology Dependence of the Correlations*

To further assess the physical origin of the correlations, we divide the sample into three broad morphological classes: early-type spirals (S0–Sb), late-type spirals (Sbc–Sdm), and irregular systems (Sm–BCD). The robustness of the correlations in each subsample is evaluated using bootstrap resampling (10^6 realizations) and non-parametric permutation tests (10^8 realizations).

The results show that the strongest and most stable correlations are obtained for late-type spirals. In this class, the $g - r$ and NUV–r colors remain strongly correlated, with Spearman coefficients of order $\rho \sim 0.57$–0.60 and permutation-based significances of ~ 4.6–4.8σ. The $r - z$ correlation remains significant at the $\sim 3.1\sigma$ level, while FUV–NUV shows a

weaker anticorrelation, significant at only $\sim 2.4\sigma$ (see Table 12).

In contrast, the early-type and irregular subsamples do not exhibit statistically significant monotonic correlations. Their bootstrap distributions are broader, sign-flip fractions are substantially larger, and permutation-based significances remain low. This indicates that the global ordering identified in the full sample is largely driven by late-type spirals and is not uniformly present across all morphological classes.

Taken together, these results show that morphology does not appear to be the primary driver of the observed correlations, but strongly modulates their detectability. The dominant signal is primarily carried by late-type spiral galaxies, while early-type and irregular systems display weaker or absent ordering relations.

Table 12. Morphology-dependent correlation analysis based on Pearson and Spearman correlation coefficients. Significances are derived from permutation tests (10^8 realizations).

	N	r_P	σ_P	ρ_S	σ_S
Early-type (S0–Sb)					
FUV–NUV	25	-0.048	0.35	0.200	0.96
$r-z$	20	0.325	1.40	0.370	1.60
$g-r$	20	0.382	1.65	0.090	0.38
NUV–r	18	0.204	0.82	0.327	1.33
Late-type (Sbc–Sdm)					
FUV–NUV	58	-0.355	2.73	-0.315	2.40
$r-z$	59	0.348	2.85	0.403	3.13
$g-r$	58	0.570	4.56	0.572	4.61
NUV–r	55	0.560	4.40	0.604	4.78
Irregular (Sm–BCD)					
FUV–NUV	53	0.191	1.36	0.171	1.23
$r-z$	50	-0.068	0.47	-0.036	0.25
$g-r$	50	0.075	0.52	0.125	0.86
NUV–r	46	0.257	1.72	0.215	1.44

7. Discussion

The results presented in this work indicate that a significant fraction of the ordering of stellar populations can be recovered from galactic dynamics through the reconstruction procedure. The existence of strong and statistically robust correlations between predicted and observed photometric quantities indicates that the dynamical mass distribution appears to encode non-trivial information about the underlying stellar population structure, including well-known large-scale trends in galaxy colors (Baldry *et al.*, 2004). This connection is consistent with the known dependence of galaxy colors and stellar populations on star formation history and structural properties (Kennicutt, 1998; Blanton & Moustakas, 2009).

A key aspect of this result is that it relies on a physically grounded construction of the gravitational binding energy, which provides a fundamental link between the mass distribution and the reconstructed stellar populations.

Beyond its implications for the nature of dark mass, this result introduces a practical tool for reconstructing stellar populations from dynamical data alone. The proposed framework provides, at each radius, a mapping between the effective mass distribution and the mixture of stellar populations required to reproduce it. This allows the inference of population gradients without relying directly on photometric measurements, but instead using the dynamical structure of the system as the primary input.

This reconstruction provides an alternative probe of stellar populations based on the gravitational structure of galaxies, and does not rely on a specific radial scale, as the selected solutions are distributed across the full extent of the disk.

The recovery of these correlations is non-trivial and depends strongly on the reconstruction procedure. In particular, the greedy algorithm enforces the dynamical constraint in a structured manner, allowing the system to converge toward configurations that are consistent with both the mass distribution and the photometric ordering.

The results also clarify that the recovered relations cannot be fully reduced to simple mass–color scaling laws. While global correlations between mass and photometric properties are well established (Bell & de Jong, 2001), the present approach reconstructs a monotonic ordering in rank space that is preserved across multiple observables and subsamples. The robustness of this ordering under bootstrap resampling, permutation tests, and morphological or inclination splits indicates that it is not driven by statistical fluctuations or trivial observational biases.

This interpretation is further supported by controlled experiments and robustness tests, which show that the correlations do not arise from the initial conditions or from the allowed parameter space alone, but emerge only when the dynamical constraint is actively enforced.

The limits of this reconstruction are also informative. In particular, the ultraviolet FUV–NUV color shows weaker and more complex behavior, reflecting the sensitivity of this observable to recent star formation and stochastic processes. Similarly, the

dependence on morphology indicates that the coupling between dynamics and stellar populations is strongest in late-type systems, where the structure of the galaxy is more regular.

A central element of the present approach is the use of a physically motivated estimator based on the gravitational binding energy of the system. This provides a physically motivated link between the mass distribution and the reconstructed stellar populations, without relying on empirical fitting relations.

In this context, the effective dark mass component inferred from galactic dynamics can be interpreted, at least in part, as gravitational binding energy. The additional mass required to explain rotation curves may therefore reflect the energy stored in the gravitational field itself, rather than an independent matter component.

8. Conclusion

We have shown that the dynamical mass distribution of galaxies contains enough information to reconstruct a significant fraction of the ordering of stellar populations. This result is obtained through the combination of a physically motivated estimator of gravitational binding energy, a structured reconstruction procedure, and extensive controlled experiments and robustness tests.

The resulting correlations are robust across multiple bands and subsamples, and are unlikely to be explained by simple relations or observational systematics. The persistence of monotonic ordering in rank space, together with its stability under bootstrap resampling and permutation tests, indicates that galactic dynamics encodes information about stellar population structure. Importantly, the selected solutions span the full extent of the disk, indicating that the recovered ordering is not tied to a specific region but reflects the global dynamical structure of galaxies.

Beyond these correlations, the proposed framework provides a practical method to infer stellar population mixtures at arbitrary radii directly from dynamical data. This opens the possibility of using galactic rotation curves as a complementary probe of stellar populations, independent of photometric measurements and their associated uncertainties. Such an approach may be particularly valuable in regimes where photometric data are incomplete or affected by strong systematics.

The limits of the reconstruction are also informative. The weaker and more complex behavior observed in the ultraviolet regime highlights the role of additional physical processes, such as recent star formation and stochastic effects, which are not fully captured by the global dynamical structure. Similarly, the dependence on morphology indicates that the coupling between dynamics and stellar populations is strongest in systems with regular structure, such as late-type spirals.

These results support a physical interpretation in which the effective dark mass component inferred from galactic dynamics appears to be closely related to gravitational binding energy. In this picture, part of the mass required to explain rotation curves can emerge naturally from the energy stored in the gravitational field, providing a direct link between dynamics and stellar population properties.

While the present work demonstrates that gravitational binding energy provides a consistent and predictive link between galactic dynamics and stellar populations, it does not yet constitute a complete alternative to standard cosmological models, and several important questions remain open. In particular, the extent to which this effective energy can fully account for the dark mass component across all astrophysical environments, including galaxy clusters and cosmological scales, remains to be established. Moreover, the connection between this effective mass and relativistic definitions of gravitational energy warrants further investigation. Extending the present framework to larger samples, higher redshift systems, and fully cosmological contexts, as well as testing its compatibility with cosmological observations, will be essential to assess its broader implications and to determine whether gravitational binding energy can constitute a complete alternative to particle dark matter.

Software Availability

The C++ program used to perform all numerical calculations and generate the corresponding graphs are freely available at `dark-mass-generator.sourceforge.io` or at `doi.org/10.6084/m9.figshare.31894372`.

Declarations

Funding — This research received no specific grant from any funding agency in the public, commercial, or not-for-profit sectors.
Competing interests — The author declares no competing interests.
Ethics approval / Consent — Not applicable.
Data and materials availability — See “Software availability”.
Author contribution – N.P. conceived the study, performed the analysis, and wrote the manuscript.

Appendix A. Raw Predicted Versus Observed Color Relations

For completeness, we present in this appendix the direct scatter plots between predicted and observed global colors, shown in linear (non–ranked) space (Figures 8). These figures complement the rank–rank analysis discussed in the main text by illustrating the dispersion and non–linear structure of the relations in absolute color units.

While the absolute correlations are weaker than their rank–based counterparts, these diagrams provide a visual reference for the intrinsic scatter, saturation effects, and non–Gaussian features present in the data.

These plots highlight the substantial intrinsic scatter in absolute color space, motivating the use of rank–based statistics in the main analysis.

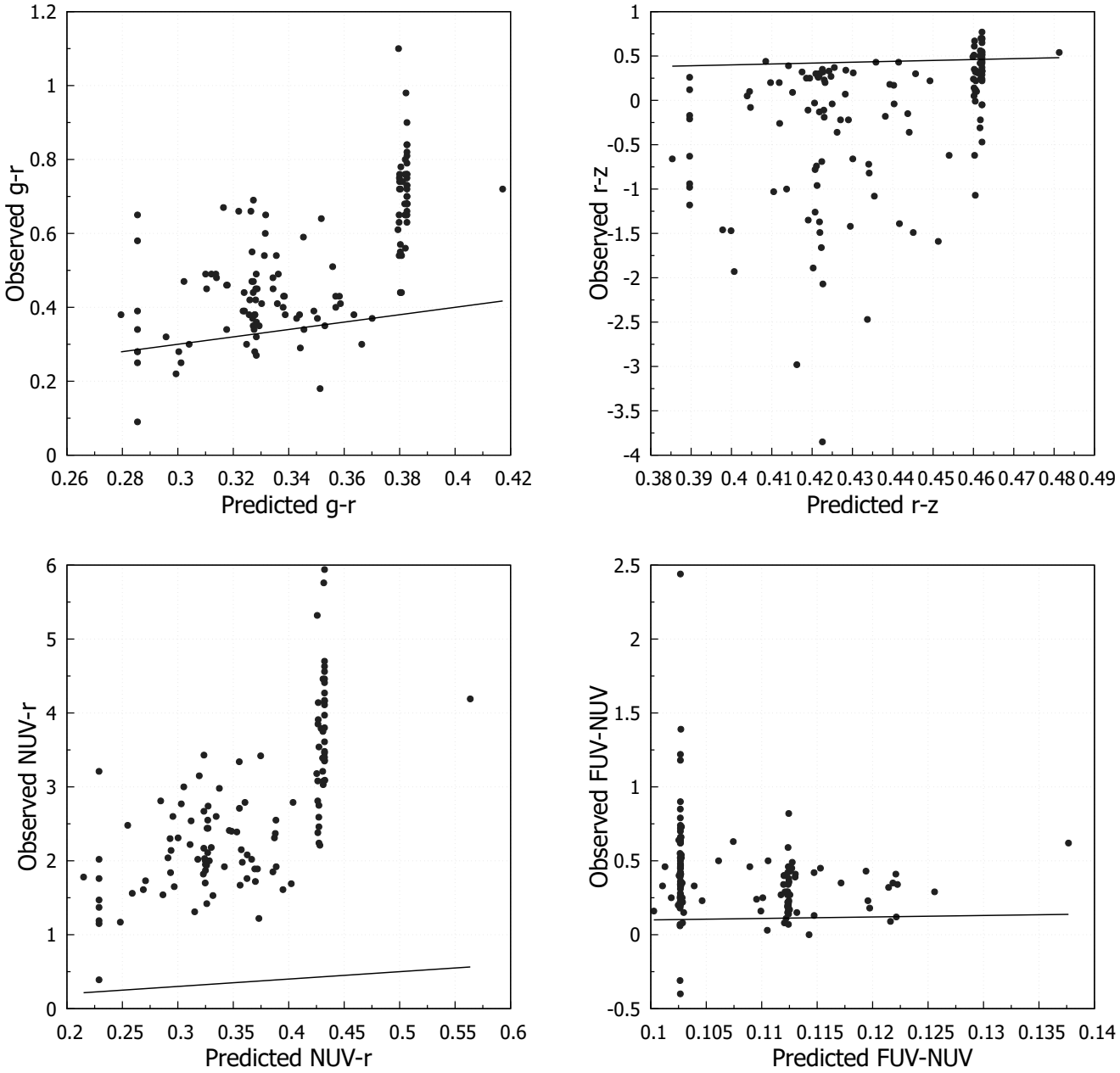

Figure 8. Predicted versus observed colors for different bands. Top: $g - r$ and $r - z$. Bottom: NUV$-r$ and FUV–NUV. The diagonal line corresponds to the identity relation $y = x$ and is shown only as a visual reference for absolute agreement.

References

Baldry, I. K., Glazebrook, K., Brinkmann, J., *et al*. 2004, The Astrophysical Journal, 600, 681

Bell, E. F., & de Jong, R. S. 2001, The Astrophysical Journal, 550, 212

Bianchi, L., *et al*. 2011, GALEX GR5 x SDSS DR7 matched catalogs, MAST / STScI High-Level Science Products, uV and UV-optical matched source catalogs

Blanton, M. R., & Moustakas, J. 2009, Annual Review of Astronomy and Astrophysics, 47, 159

Brillouin, L. 1964, Journal de Physique, 25, 883

—. 1965, Proceedings of the National Academy of Sciences of the United States of America, 53

Bruzual, G., & Charlot, S. 2003, Monthly Notices of the Royal Astronomical Society, 344, 1000

Conroy, C. 2013, Annual Review of Astronomy and Astrophysics, 51, 393

Conroy, C., Gunn, J. E., & White, M. 2009, The Astrophysical Journal, 699, 486

Courteau, S., *et al*. 2014, Reviews of Modern Physics, 86, 47

Deur, A. 2019, European Physical Journal C, 79, 883

—. 2021, European Physical Journal C, 81, 213

—. 2022, Classical and Quantum Gravity, 39, 135003

Deur, A., Sargent, C., & Terzic, B. 2020, The Astrophysical Journal, 896, 94

Efron, B., & Tibshirani, R. J. 1993, An Introduction to the Bootstrap (Chapman and Hall/CRC)

Fukugita, M., Ichikawa, T., Gunn, J. E., *et al*. 1996, The Astronomical Journal, 111, 1748

Good, P. I. 2005, Permutation, Parametric, and Bootstrap Tests of Hypotheses, 3rd edn. (Springer)

Hawking, S. W. 1968, Journal of Mathematical Physics, 9, 598

Hayward, S. A. 1996, Physical Review D, 53, 1938

Kennicutt, R. C. 1998, Annual Review of Astronomy and Astrophysics, 36, 189

Lelli, F., McGaugh, S. S., & Schombert, J. M. 2016, The Astronomical Journal, 152, 157

Martin, D. C., *et al*. 2005, The Astrophysical Journal Letters, 619, L1

McGaugh, S. S., Lelli, F., & Schombert, J. M. 2016, Physical Review Letters, 117, 201101

McGaugh, S. S., Schombert, J. M., Bothun, G. D., & de Blok, W. J. G. 2000, The Astrophysical Journal, 533, L99

Misner, C. W., & Sharp, D. H. 1964, Physical Review, 136, B571

Pearson, K. 1895, Proceedings of the Royal Society of London, 58, 240

Persic, M., Salucci, P., & Stel, F. 1996, Monthly Notices of the Royal Astronomical Society, 281, 27

Poupart, N. 2014, General Science Journal, available online at General Science Journal

—. 2017a, General Science Journal, available online at General Science Journal

—. 2017b, General Science Journal, available online at General Science Journal

—. 2025, Dark Mass is Potential Energy, Preprint available at FigShare (doi.org/10.6084/m9.figshare.30543407) and ResearchGate (doi.org/10.13140/RG.2.2.15355.43046)

—. 2026, Foundations for Gravitational Potential Energy Evaluation, Preprint available at FigShare (https://doi.org/10.6084/m9.figshare.31320772) and ResearchGate (doi.org/10.13140/RG.2.2.14829.04323)

Quenouille, M. H. 1949, Journal of the Royal Statistical Society. Series B, 11, 68

Rubin, V. C., Ford, W. Kent, J., & Thonnard, N. 1980, The Astrophysical Journal, 238, 471

Spearman, C. 1904, The American Journal of Psychology, 15, 72

Taylor, E. N., *et al*. 2011, Monthly Notices of the Royal Astronomical Society, 418, 1587

Tukey, J. W. 1958, Annals of Mathematical Statistics, 29, 614

Tully, R. B., Pierce, M. J., Huang, J.-S., *et al*. 1998, The Astronomical Journal, 115, 2264

York, D. G., *et al*. 2000, The Astronomical Journal, 120, 1579